nature communications

Article

https://doi.org/10.1038/s41467-025-57329-0

Scalable and efficient electrochemical bromination of arenes with Faradaic efficiencies surpassing 90%

Received: 2 July 2024

Accepted: 13 February 2025

Bing Zhang[1,2,7], Wei Liu[1,7], Zhu Liu[2], Yuhou Pei[2], Di Li[2], Hongbin Yang[3], Chuntian Qiu[1,2], Yang Fan[1], Yinghua Xu[4], Jie Ding[3], Lei Yu[5], Bin Liu[3] & Chenliang Su[1,6]

Developing cost-effective and environmentally friendly approaches to synthesize brominated chemicals, which are important intermediates for the synthesis of various useful molecules such as pharmaceuticals, surfactants, pesticides, and biologically active heterocyclic compounds, is of great significance. Herein, we present a highly efficient electrochemical bromine evolution reaction over vacancy rich Co_3O_4 using cheap NaBr as the bromine source for the synthesis of valuable brominated fine chemicals and pharmaceuticals under ambient conditions. The introduction of oxygen vacancy onto Co_3O_4 can greatly enhance the activity and selectivity of bromine evolution reaction by optimizing Br* intermediate adsorption and desorption, enabling bromination of a series of bioactive molecules and pharmaceuticals at high yields.

Brominated chemicals are versatile intermediates for synthesizing value-added fine chemicals and pharmaceuticals[1–6]. For example, *p*-bromo-anisole, with a consumption of more than 20,000 tons per year in China, is widely served as the basic molecule to combine with other functional groups via the well-known Suzuki-coupling reaction. 4-Bromo-3-methylanisole (10,000 T/a in China) is the intermediate to make colorant. Bromoxynil octanoate (150,000 T/a in the world) is the main herbicide. Owing to the unique function of bromine, demands for late-stage bromination of bioactive molecules and pharmaceuticals to regulate their physicochemical properties, such as pK_a and metabolic rate, are rapidly going up[6–9]. The current strategies of bromination rely heavily on liquid Br_2; more than 0.5 million tons of liquid Br_2 are consumed each year globally that are produced via traditional high energy consumption and high discharge processes[4]. Liquid bromine can ensure fast bromination reactions, but suffers from poor bromination selectivity and the unavoidable generation and release of equimolar HBr, causing poor atom-efficiency and bringing serious environmental pollution. The pungent odor as well as the corrosive nature largely hinder its transportation, storage, and handling processes for practical applications[3]. NBS (*N*-bromosuccimimide) can fulfill bromination with moderate reaction rates, which is, unfortunately, derived from liquid Br_2[10]. Besides, the stability of NBS is problematic as it is sensitive to light, water, and reductive reagents[10,11].

The electrochemical method offers an interesting approach to synthesize bromine for bromination reaction[6,8,9]. The electrochemical strategy, driven by electricity, is commonly operated under mild conditions without the requirement of strong or toxic redox reagents[12–14], which is considered as a promising sustainable technology to enable a green industry for useful chemicals and/or pharmaceuticals synthesis in the coming carbon-neutral century. Owing to a

---

[1]International Collaborative Laboratory of 2D Materials for Optoelectronics Science and Technology of Ministry of Education, Institute of Microscale Optoelectronics, Shenzhen University, Shenzhen, China. [2]ZJU-Hangzhou Global Scientific and Technological Innovation Center, Zhejiang University, Hangzhou, China. [3]Department of Materials Science and Engineering, Department of Chemistry, Hong Kong Institute for Clean Energy (HKICE) & Center of Super Diamond and Advanced Films (COSDAF), City University of Hong Kong, Hong Kong, SAR, China. [4]College of Chemical Engineering, Zhejiang University of Technology, Hangzhou, China. [5]College of Chemistry and Chemical Engineering, Yangzhou University, Yangzhou, China. [6]State Key Laboratory of Radio Frequency Heterogeneous Integration, Shenzhen University, Shenzhen, China. [7]These authors contributed equally: Bing Zhang, Wei Liu.
e-mail: bliu48@cityu.edu.hk; chmsuc@szu.edu.cn

spatially-decoupled redox system at anode and cathode, accurate electrochemical windows and real-time electrochemical signals can ensure good reaction selectivity and high energy efficiency[15]. More importantly, the ease of scaling up electrochemical cells facilitates the large-scale production of chemicals or pharmaceuticals via electrochemical synthesis[13]. Over the past decades, various electrochemical syntheses have been developed to produce brominated organic molecules using bromide salt as the green bromine source[16–23]. Commercial electrodes such as carbon, Pt was roughly applied as the anode in an electrochemical cell to drive an electrochemical Br^- oxidation reaction to in-situ produce Br_2 to brominate organic molecules, which suffers from very high overpotential, poor-Faradaic efficiency and substrate over-oxidation (Supplementary Table 1). It is thus urgent to deeply understand the mechanism of electrochemical bromine evolution reaction (BER) and then guide the rational design of suitable catalytic materials for high-performance BER.

In this work, we fabricated an oxygen-vacancy-rich Co_3O_4 catalyst that exhibits high bromine selectivity and reaction rate at room temperature in air to synthesize Br substituted molecules, natural products, and drugs using NaBr as the cheap bromine source. It delivers ultralow operating potential within 50 mV to catalyze BER at 10 mA cm^{-2}. These enable the substitution of oxygen evolution reaction (OER) by BER to couple with hydrogen evolution reaction (HER) for energy-saving electrochemical hydrogen production (Supplementary Fig. 1, 2). Based on a collection of electrochemical and in-situ spectroscopic measurements together with density functional theory (DFT) calculations, it is found that the oxygen vacancy on Co_3O_4 can effectively regulate the adsorption and desorption of Br^* to promote BER at low overpotentials. The in-situ produced Br_2 works very effectively in the bromination of arenes, achieving overall bromination Faradaic efficiencies greater than 90%. The as-developed electrochemical bromine evolution approach can be easily scaled up to synthesize a kilogram scale of bioactive molecules.

Results

Catalyst preparation and characterization

Electrodeposition combined with calcination (Fig. 1a) was applied to prepare oxygen-vacancy-rich cobalt oxide on carbon paper (Co-O_V@CP). The carbon paper (CP) is made of carbon fibers with diameters of several micrometers. $Co(OH)_2$ was electrodeposited on CP (Supplementary Fig. 3a) followed by calcination in a tube furnace to form black pristine Co_3O_4 nanosheets (Co_3O_4@CP). Further calcination in a 5% H_2/Ar atmosphere at 300 °C for 15 min created oxygen vacancies on the surface of Co_3O_4 nanosheets (Co-O_V@CP) (Fig. 1b–g)[24,25] and the mass loading of Co on carbon paper is determined to be about 4.65 mg cm^{-2} (by ICP-MS, Supplementary Table 2). Both Co_3O_4@CP and Co-O_V@CP display ultrathin honeycomb-like nanosheet arrays on CP (Supplementary Fig. 3b, c)[26]. The elemental mapping results reveal uniform distribution of Co and O elements across the nanosheet framework (Fig. 1d, e and Supplementary Fig. 3). High-resolution transmission electron microscopy (TEM) images show clear lattice spacings that can be indexed to the (220) plane of cubic Co_3O_4. The atomic discontinuity near the Co_3O_4 crystal lattice may be due to the formation of oxygen vacancies[27,28].

The crystal structure of Co_3O_4@CP and Co-O_V@CP were examined by X-ray diffraction (XRD). As shown in Supplementary Fig. 4, the diffraction peaks at 31.4°, 36.9°, 44.9°, 59.3° and 65.3° can be assigned to the (220), (311), (400), (511) and (440) planes of cubic Co_3O_4 (JCPDS 42-1467) and the diffraction peaks at 18.2°, 26.6° and 54.9° are resulted from CP[26,29]. It is worth noting that the diffraction peaks of Co-O_V@CP are almost identical to those of Co_3O_4@CP, suggesting minimum bulk crystal structure change before and after H_2 treatment (the short-time reduction treatment only induces formation of oxygen vacancies on surface of Co_3O_4 (Fig. 1f, g)). Electron paramagnetic resonance (EPR) measurements (Fig. 1h) show an enhanced EPR signal at $g = 2.0045$ for Co-O_V@CP, which can be attributed to more unpaired electrons resulting from Co^{2+}, suggesting the presence of abundant oxygen vacancies on the surface of Co-O_V@CP[30,31]. The oxygen vacancies on the surface of Co-O_V@CP were further studied by X-ray photoelectron spectroscopy (XPS). The survey spectra (Supplementary Fig. 5a) show both Co and O on the surface of Co_3O_4@CP and Co-O_V@CP. The high-resolution Co 2*p* XPS spectra (Supplementary Fig. 5b) exhibit two peaks at around 780 and 796 eV, which can be attributed to Co $2p_{3/2}$ and Co $2p_{1/2}$, respectively. Compared to Co_3O_4@CP, the Co-O_V@CP displays two new satellite peaks centered at 786 and 803 eV, which may be due to the reduction of Co^{3+} to Co^{2+} along with the generation of oxygen vacancies. The high-resolution O 1*s* XPS spectra, as shown in Fig. 1i further verify the existence of oxygen vacancies on Co-O_V@CP. The deconvoluted peaks at 529.6, 531.2, and 532.8 eV are attributed to the lattice oxygen, the oxygen vacancy, and the adsorbed hydroxyl species, respectively[26–28,32–35]. The obviously decreased lattice oxygen peak (529.6 eV) and enhanced oxygen vacancy peak (531.2 eV) indicate a higher concentration of oxygen vacancies on the surface of Co-O_V@CP. The concentration of surficial oxygen vacancies was estimated according to the deconvoluted O 1*s* XPS peaks. By considering the coordination number of Co (binding with six O atoms; oxygen vacancy may increase fivefold formation of Co(Ov)-O)) with O (binding with four Co atoms; oxygen vacancy may induce triple decrease of Co-O bond) atoms as well as the increased or decreased percentage of Co-O or Co(Ov)-O compared with the total oxygen bonding with Co or Co(Ov) before H_2 treatment, the content of surficial oxygen vacancies was determined to be in the range of 6%-8% (Fig. 1j).

Electrocatalytic performance

The electrochemical BER on Co_3O_4@CP and Co-O_V@CP were probed by linear sweep voltammetry (LSV) in a three-electrode configuration. As displayed in Fig. 2a, the onset potential of the anodic oxidation reaction is clearly decreased from 1.12 V vs. SCE in Na_2SO_4 electrolyte to 0.82 V vs. SCE in NaBr electrolyte due to the more sluggish four-electron-transfer OER as compared to the two-electron-transfer BER. The Co-O_V@CP electrode only requires a potential as low as 0.89 V vs. SCE to drive BER at a current density of 10 mA/cm^2 in 0.5 M NaBr aqueous solution, which is 320 mV lower than that of OER in Na_2SO_4 electrolyte. Considering that a large amount of the electricity to overcome the high overpotential is consumed by OER during water electrolysis[36,37], the BER coupled hydrogen production can decrease 30% of the total electricity consumption. Besides, the on-site generated Br_2 from BER can be directly used for the synthesis of valuable Br-substituted chemicals and pharmaceuticals at ambient temperature and pressure. To create a compatible media for organic substrate and increase organic substrate solubility for the bromination reaction, acetonitrile was added into the NaBr aqueous solution. As shown in Fig. 2b, it can be seen that the addition of organic substrate into the NaBr electrolyte does not shift the LSV curve of bare glassy carbon (GC) electrode. Thus, optimizing the surface property of BER electrocatalyst is expected to improve the effectiveness of the bromination reaction. Both Co_3O_4@CP and Co-O_V@CP show much enhanced BER activity as compared to CP, among which, Co-O_V@CP displays the lowest BER onset potential at 0.82 V vs. SCE, which is about 50 mV and 150 mV lower as compared to Co_3O_4@CP and pristine CP, respectively (Fig. 2c and Supplementary Fig. 6). We made the corresponding Tafel plots using the iR corrected LSV curves. The Tafel slope for Co-O_V@CP is estimated to be ~48 mV dec^{-1}, suggesting favorable kinetics for the two-electron transfer Br^- oxidation over Co-O_V@CP. While the Tafel slope (Fig. 2d) for Co_3O_4@CP is calculated to be ~114 mV dec^{-1}, indicating relatively sluggish Br^- oxidation on Co_3O_4@CP[38,39]. Next, an electrolysis system coupling the Co-O_V@CP-catalyzed BER with cathodic HER was established to verify the feasibility of substituting OER by BER to couple with HER for energy-saving hydrogen production. We evaluated the Faradaic efficiency (FE) for hydrogen

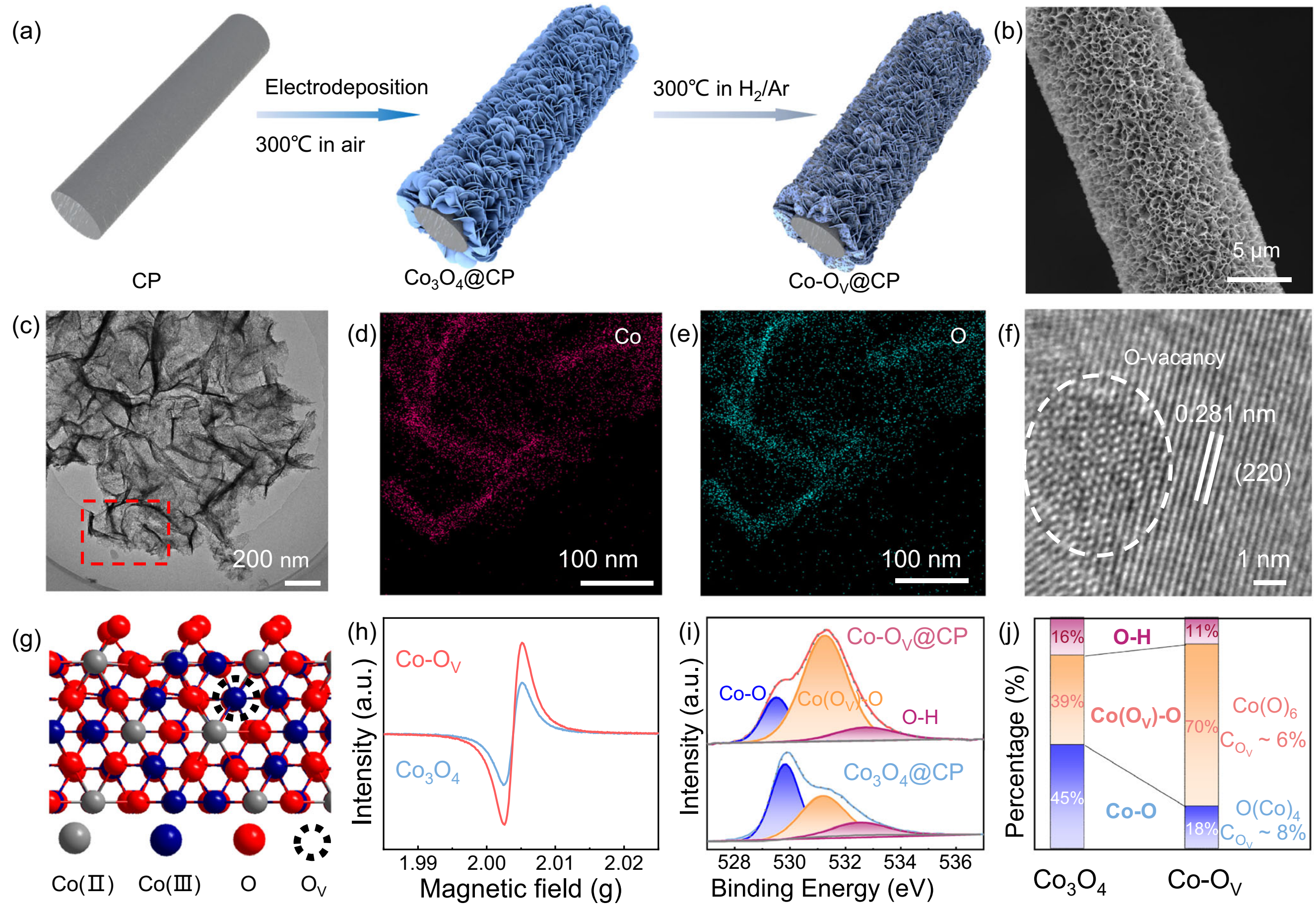

Fig. 1 | Catalyst preparation and characterization. a Schematic illustration showing preparation of Co-O_V@CP. Typical SEM (**b**) and TEM (**c**) images of Co-O_V and the corresponding elemental distribution of Co (**d**) and O (**e**). HRTEM image (**f**) and schematic crystal structure (**g**) of Co-O_V. (**h**) EPR spectra, (**i**) O 1*s* XPS spectra and (**j**) the estimated surface oxygen vacancy content.

production, and the measured volume of produced H_2 gas matched well with the theoretical value (Supplementary Fig. 7), reaching a FE_{H2} as high as more than 99%. The possible products in the liquid phase were examined by NMR. As depicted in Supplementary Fig. 8, the NMR peaks at around 2.0 and 4.7 ppm of chemical shifts could be assigned to CH_3CN and D_2O, with no detectable peaks originating from CH_3CN decomposition products, indicating the stability of acetonitrile in electrolysis.

We then optimized the solvent and the concentration of NaBr for electrochemical bromination of anisole at a constant applied potential of 1.1 V vs. SCE on Co-O_V@CP. The mixture of equal volume of 0.5 M NaBr aqueous solution and acetonitrile was found to give the best performance in electrochemical bromination of anisole. Besides, the yield of Br substituted anisole varied with respect to the applied potential and pH of the reaction environment (Fig. 2e). Neutral reaction media favored the electrochemical bromination reaction. Less than 40% yield was obtained at 0.9 V vs. SCE after 4 h in neutral electrolyte and the yield increased to 94% if the applied potential was increased to 1.1 V vs. SCE. These results directly indicate that the Br_2 generation rate determines the total electrochemical bromination rate, which can help us conclude that the bromination reaction is rate-limited at the oxidation of Br^-. Faradaic efficiency (FE) offers a key parameter to assess the selectivity of electrochemical reaction. The FE for the formation of Br substituted anisole increased from 69.1% to ~91.6% with increasing applied anodic potential from 0.9 to 1.1 V vs. SCE within 2 h, while decreased gradually to 83.1% if the applied potential further increased to 1.3 V vs. SCE due to promoted OER (Fig. 2f). The FEs on Co_3O_4@CP show the same potential dependence, but are lower than those on Co-O_V@CP across the entire potential window. Besides activity and selectivity, the Co-O_V@CP electrode also displays good stability (Fig. 2g). Compared to the reported commercial electrodes such as carbon[20], Pt[19,21] and RuO_2[22] electrodes, the Co-O_V@CP electrode requires a much less overpotential to drive BER (Fig. 2g inset, Supplementary Table 1). The stability of Co-O_V@CP can be further verified by cyclic electrochemical bromination experiments. Within four cycles of Br substituted anisole electrosynthesis over Co-O_V@CP at 1.1 V vs. SCE, stable yield of more than 90% could be achieved (Fig. 2h). After electrochemical reaction, the Co-O_V@CP electrode was examined by XPS and XRD (Supplementary Fig. 9–11), which displayed well-preserved crystal structure and valence states, and the surface oxygen vacancy signals of Co(O_V)-O on the Co_3O_4-O_v catalyst remained almost unchanged, indicating good stability of this catalyst. Furthermore, we can make the electrochemical bromination reaction portable for on-site production of Br substituted chemicals through powering the electrosynthesis cell by commercial solar cells as demonstrated in Fig. 2i. This strategy is attractive that can transform solar energy into chemical bonds for green organic synthesis through the photovoltaic conversion.

Mechanistic studies

To dig out the excellent BER performance over Co-O_V@CP, we estimated ECSA of Co-O_V@CP and Co_3O_4@CP samples as shown in Supplementary Fig. 12. The ECSA of Co-O_V@CP is only slightly increased as compared to that of Co_3O_4@CP. We then performed in-situ Raman

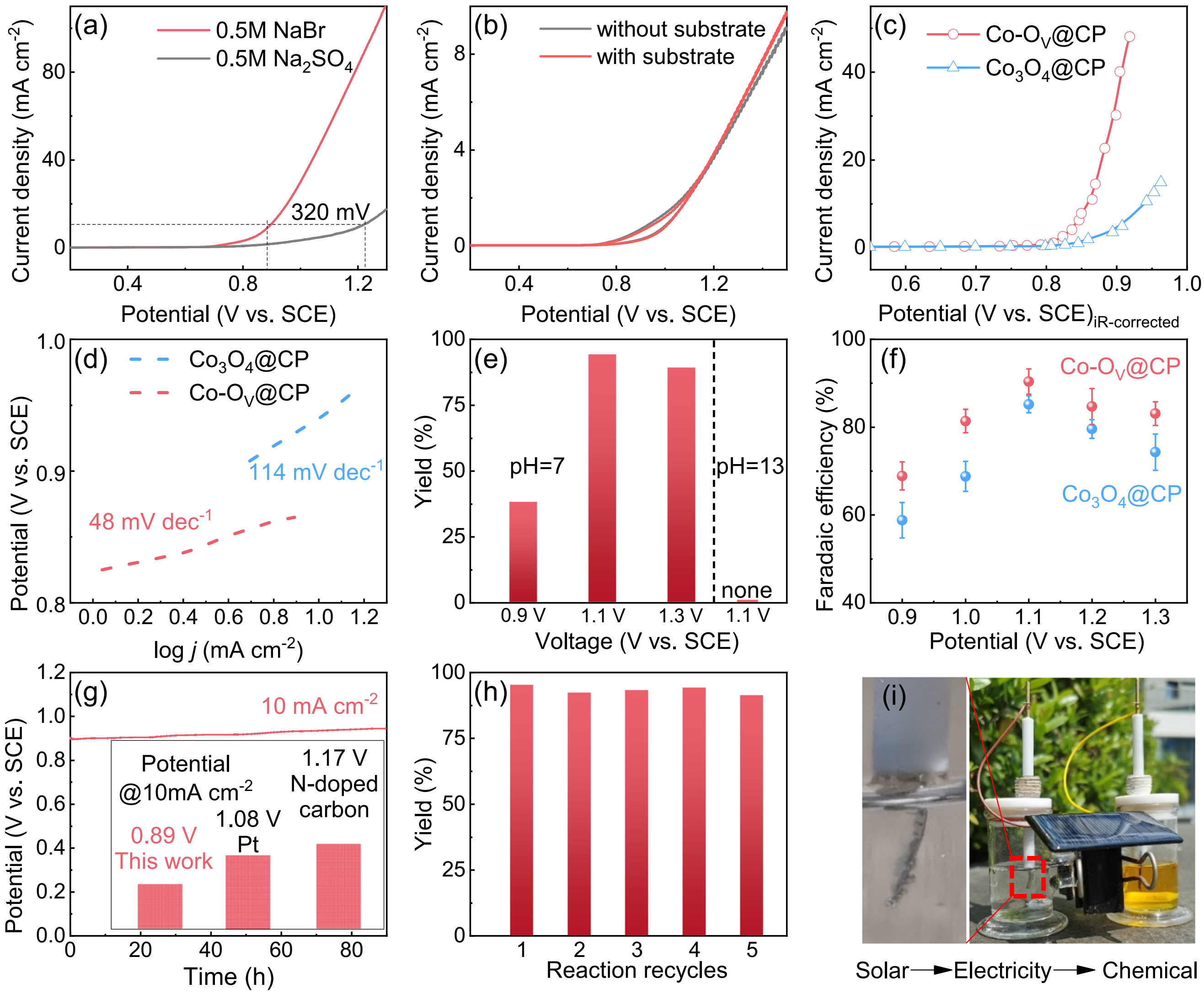

Fig. 2 | Electrochemical measurements. a LSV curves of Co-O_V@CP recorded in 0.5 M Na_2SO_4 and 0.5 M NaBr aqueous solution, respectively. **b** CV curves recorded on glassy carbon (GC) electrode in 5 ml acetonitrile plus 5 ml 0.5 M NaBr aqueous solution with or without anisole as substrate. Scan rate: 100 mV/s. iR-corrected LSV curves (**c**) and the corresponding Tafel plots (**d**) in 0.5 M NaBr aqueous solution. Yields (**e**) and FE values (**f**) for bromination of anisole on Co-O_V@CP and Co_3O_4@CP at different bias potentials. Potentiometric curve for electrochemical BER (**g**) (inset compares the applied potential[20–22] required to drive BER at a current density of 10 mA cm^{-2}) and cyclic bromination experiments (**h**) over Co-O_V@CP. **i** Digital photograph showing a sunlight-driven electrochemical bromination cell using Co-O_V@CP as the anode. The error bars correspond to data from three independent experiments.

spectroscopy measurements. As shown in Fig. 3a, the in-situ Raman spectra well illustrate the potential-dependent Br^- adsorption in 0.5 M NaBr aqueous solution. Recorded on Co_3O_4@CP, the peak at 692 cm^{-1} with A_{1g} symmetry originates from the octahedral CoO_6 sites in crystalline Co_3O_4. The intensity of this A_{1g} peak as well as E_g (487 cm^{-1}) and F_{2g} (529 cm^{-1}) peaks over Co_3O_4@CP keeps nearly unchanged with increasing applied anodic potential (Fig. 3a and Supplementary Fig. 13a)[40–42]. Over Co-O_V@CP, A_{1g}, E_g and F_{2g} peaks can also be clearly observed in the Raman spectra (Fig. 3b and Supplementary Fig. 13b), indicating that mild H_2 reduction treatment would not damage the bulk Co_3O_4 spinel structure[41]. The new vibrational peak at 378 cm^{-1} compared with that in 0.5 M Na_2SO_4 aqueous solution (Supplementary Fig. 14) can be identified in the in-situ Raman spectra as the A_g phonon mode of Co-Br bond[43,44], whose intensity varies insignificantly on Co_3O_4@CP while gradually decreases on Co-O_V@CP with increasing applied anodic potential, indicating possibly easier desorption of *Br species on Co-O_V@CP than on Co_3O_4@CP. Considering that the Co-O vibration in the as-developed electrocatalysts is quite stable during BER, the Co-Br to Co-O peak intensity ratio is able to tell the relative *Br coverage under the reaction conditions (Fig. 3c). Specifically, the peak intensity of the Co-Br vibration decreased by 33% when the applied bias potential increased from 0.6 to 0.8 V vs. SCE (Fig. 3c), which could be attributed to the activation of BER that accelerated desorption of adsorbed *Br on Co-O_V. Note that both Co_3O_4@CP and Co-O_V@CP display the A_g phonon mode of Co-Br even at the open circuit potential (OCP) in NaBr solution, suggesting spontaneous adsorption of Br^-. Density functional theory (DFT) calculation was then performed to study the Br^- adsorption and BER process. As shown in Fig. 3d-f and Supplementary Fig. 15, the adsorption energy of Br^- on different sites of Co_3O_4 and Co-O_V were carefully calculated. Br^- can be easily adsorbed on spinel Co site of Co_3O_4 with Gibbs free energy of -0.74 eV, which explains the A_g phonon mode (378 cm^{-1}) of Co-Br bond observed in the in-situ Raman spectra. After introduction of oxygen vacancies, the Br^- adsorption on Co site next to the oxygen vacancy (denoted as Co(O_V), Fig. 3g) was enhanced and showed a favorable adsorption energy of -0.79 eV. The adsorption of Br^- over Co_3O_4@CP and Co-O_V@CP in NaBr

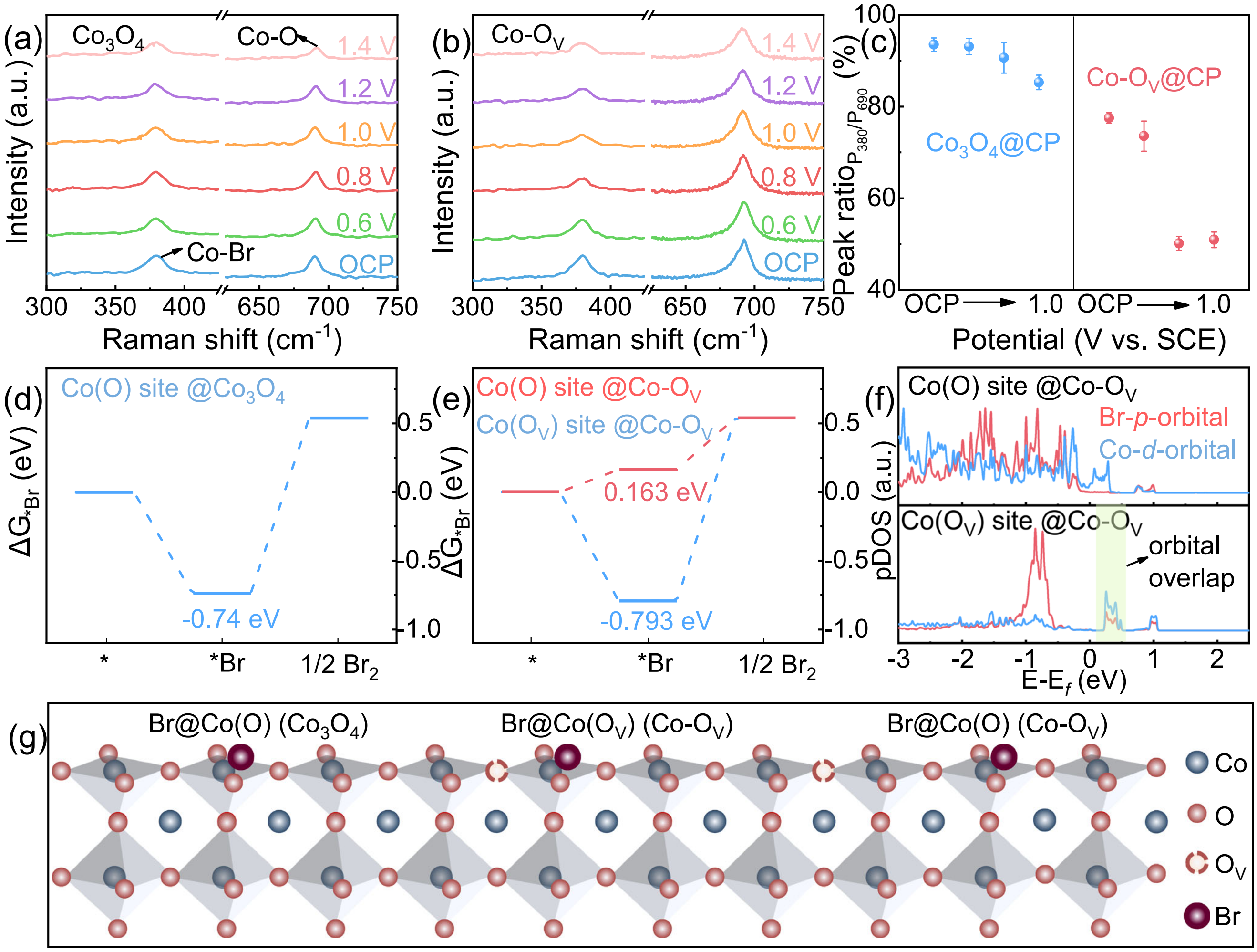

Fig. 3 | Reaction mechanism. In-situ Raman spectra for BER recorded on Co_3O_4@CP (**a**) and Co-O_V@CP (**b**) at different bias potentials (potential vs. SCE). **c** The in-situ Raman peak intensity for Co-Br vibration at 380 cm^{-1} recorded on Co_3O_4@CP and Co-O_V@CP at different bias potentials. The calculated adsorption energy of *Br on Co_3O_4 (**d**) and Co-O_V (**e**). Projected density of states (pDOS) of Co-O_V after adsorbing *Br on Co(O_V) site or Co (O) site (**f**). **g** Schematic illustration showing possible *Br adsorption sites on Co_3O_4 and Co-O_V samples. The error bars correspond to data from three independent measurement.

solution can be clearly observed in the XPS spectra (Supplementary Fig. 16)[45], matching well with the DFT calculation results. While Br$^-$ adsorption energy on the Co site around the oxygen vacancy (denoted as Co(O), Fig. 3g) is 0.163 eV, considering that BER involves two up-hill electron transfer processes, this moderate unfavorable adsorption of Br$^-$ may facilitate the desorption of *Br to form Br_2 over Co-O_V@CP. The desorption energy barrier for *Br over Co-O_V (also the rate-determining step of BER) is calculated to be 0.377 eV, which is much smaller than that over Co_3O_4 (1.28 eV) and matches well with the experimentally determined Tafel slope. All these results reveal that the Co site around the oxygen vacancy is likely the active site for BER over Co-O_V@CP. Considering the coordinating structure of spinel Co_3O_4: typically, four Co atoms coordinate with one oxygen atom, and one oxygen vacancy can induce four Co(O_V). The introduction of oxygen vacancies will create both strong Br adsorption sites (Co(O_V)) and weak Br adsorption sites (Co(O), Supplementary Fig. 17). This contributes to explain the peak intensity decrease of Co-Br vibration in the in-situ Raman spectra over Co-O_V@CP as shown in Fig. 3c. Removing oxygen vacancies via calcining Co-O_V@CP in air at 300 °C for 1 h greatly decreased the BER performance (Supplementary Fig. 18), highlighting the significant role of oxygen vacancy on Co_3O_4 played for the BER. Additionally, projected density of states (pDOS) of Br on different Co sites of Co-O_V were further calculated (Fig. 3f). The overlapping between Co 3*d* and Br 4*p* orbitals was observed near but above the Fermi level in the pDOS of Br-Co(O_V), revealing the possible Br-Co(O_V) covalency, while overlapping between Co 3*d* and Br 4*p* orbitals was observed below the Fermi level in the pDOS of Br-Co(O), indicating unfavorable covalency of Br-Co(O) within the oxygen vacancy-rich Co_3O_4 framework, further explaining the calculated adsorption energies and confirming the Co atom (Co(O) site) next to Co(O_V) as the active site over Co-O_V for electrochemical BER.

Under optimized reaction conditions (Supplementary Table 3), the reaction scope was carefully investigated (Fig. 4). Representative substrates bearing electron-donating or electron-withdrawing substituents such as methoxy-, methyl- or cyan- on arenes (**2a-2m**) could be efficiently converted to the corresponding brominated products (with 76-95% yields) at the most electrophilic position[6,9,10]. *Para*-position of strong electron-donating functional group is more preferrable for bromination (**2 d, 2e**), while *ortho*-position is preferred only if the *para*-position is blocked (**2b, 2c**). Sensitive functionalities including alkyne, amine, amide, ester, and ketone, were found to be well-compatible, giving the desired brominated products (e.g., **2c, 2e, 2i, 2 m** etc.) in good yields. Substrates composed of halogen substituents, such as Br- (**2j**) and Cl- (**2b**), could be smoothly brominated in high yields (90% and 88%, respectively), indicating the possibility of stepwise bromination. Dual bromination of certain substrates (e.g., **2 h**)

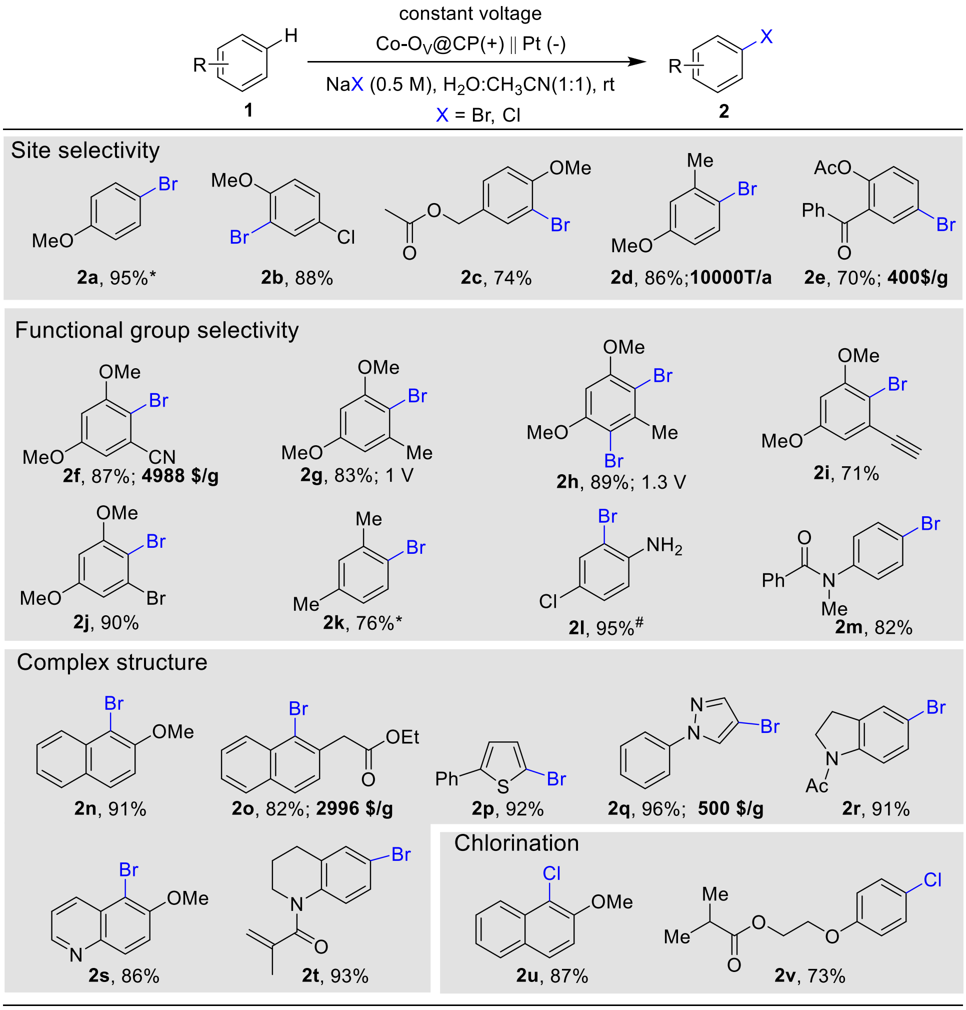

Fig. 4 | Substrate dependent electrochemical bromination/chlorination reaction. Reaction conditions: Co-O$_V$@CP (size: 10 mm × 10 mm × 0.3 mm) anode and platinum plate (size: 10 mm × 10 mm × 0.2 mm) cathode in an H-type cell divided by Nafion membrane, SCE as reference electrode; NaBr (0.5 M in deionized water, 7.5 mL), CH$_3$CN (7.5 mL) in each chamber, **1** (0.5 mmol), constant voltage (0.9–1.3 V vs. SCE) at room temperature for 4–8 h. Isolated yields are shown. *GC-MS yield. #The reaction was carried out under standard conditions for 2 h followed by adding *p*-chloroaniline (0.5 mmol).

could be achieved by increasing the applied voltage (e.g., 1.3 V vs. SCE). It is delightful to see the highly selective bromination of naphthalene derivatives, which furnished the value-added products **2n** and **2o** in good to excellent yields. Importantly, bromination of heterocyclic compounds such as thiophene (**2p**), parazole (**2q**), indoline (**2r**), quinoline (**2 s**) and 1,2,3,4-tetrahydroquinoline (**2t**) were also successfully achieved, confirming the wide compatibility of the electrochemical bromination strategy. The electrochemical bromination strategy could be further extended to chlorination (**2u**-**2v**) by simply replacing NaBr with NaCl. The Faradaic efficiency for some above products in Fig. 4 can be calculated in the range of 70–86% (Supplementary Table 4).

Late-stage bromination of natural products, drugs and their derivatives are of great significance for biological applications and drug developments[6–10] (Fig. 5). Solvents were further optimized for increasing the solubility of natural products with large molecular weight. A variety of biomolecules such as guaiacol derivative (**2w**), psoralen ether derivative (**2x**), gemfibrozil (**2 y**) and naproxen-derived methyl esters (**2z**) could be facilely brominated with excellent isolated yields. The dual bromination of a flavoring agent was demonstrated, affording 2,5-dibromide product **2aa** with 78% yield. As one type of spice, phenoxyethyl isobutyrate (**2ab**) could be brominated at the *para* position of the alkoxy functional group. Adapalene methyl ester, a more complex drug derivative, reacted smoothly to produce ortho-bromination product **2ac** in 85% yield. For δ-tocopherol derived substrate, bromination tended to take place on the less hindered position (**2ad**). This tool was also applied to deuterated biomolecules, to furnish the corresponding brominated products (**2ae-ag**), which could be served as important building blocks for the synthesis of deuterated drugs. The electrochemical bromination reaction can be easily scaled up in a flow cell system (photograph in Fig. 5, Supplementary Fig. 19). As displayed in Fig. 5, Naproxen (**2x'**), psoralen(**2z'**) and *δ*-tocopherol (**2ad'**) derivatives could be brominated to produce gram-scale products with good isolated yields, pinpointing the great potentials for flow-synthesis of valuable brominated chemicals and pharmaceuticals. Impressively, an unprecedented 0.61-kilogram-scale synthesis of brominated naproxen derivative was achieved using 4 tandem cells with an electrode area of 3 × 3.5 cm^2, illustrating the great potential for industrial-scale bromination of this method with sustainable and cheap NaBr. Compared to traditional bromination routes via Br$_2$, NBS or other non-natural bromination reagents, this strategy will benefit from unnecessary complex processes with high energy-consumption, tough transportation/storage and/or environmental unfriendliness (Supplementary Fig. 20). As can be seen from the economic analysis (inset figure in Fig. 5 and economic analysis in Supplementary Information including Supplementary Fig. 21–23 and Supplementary Tables 5, 6), the electrochemical BER route to produce 2z can save near

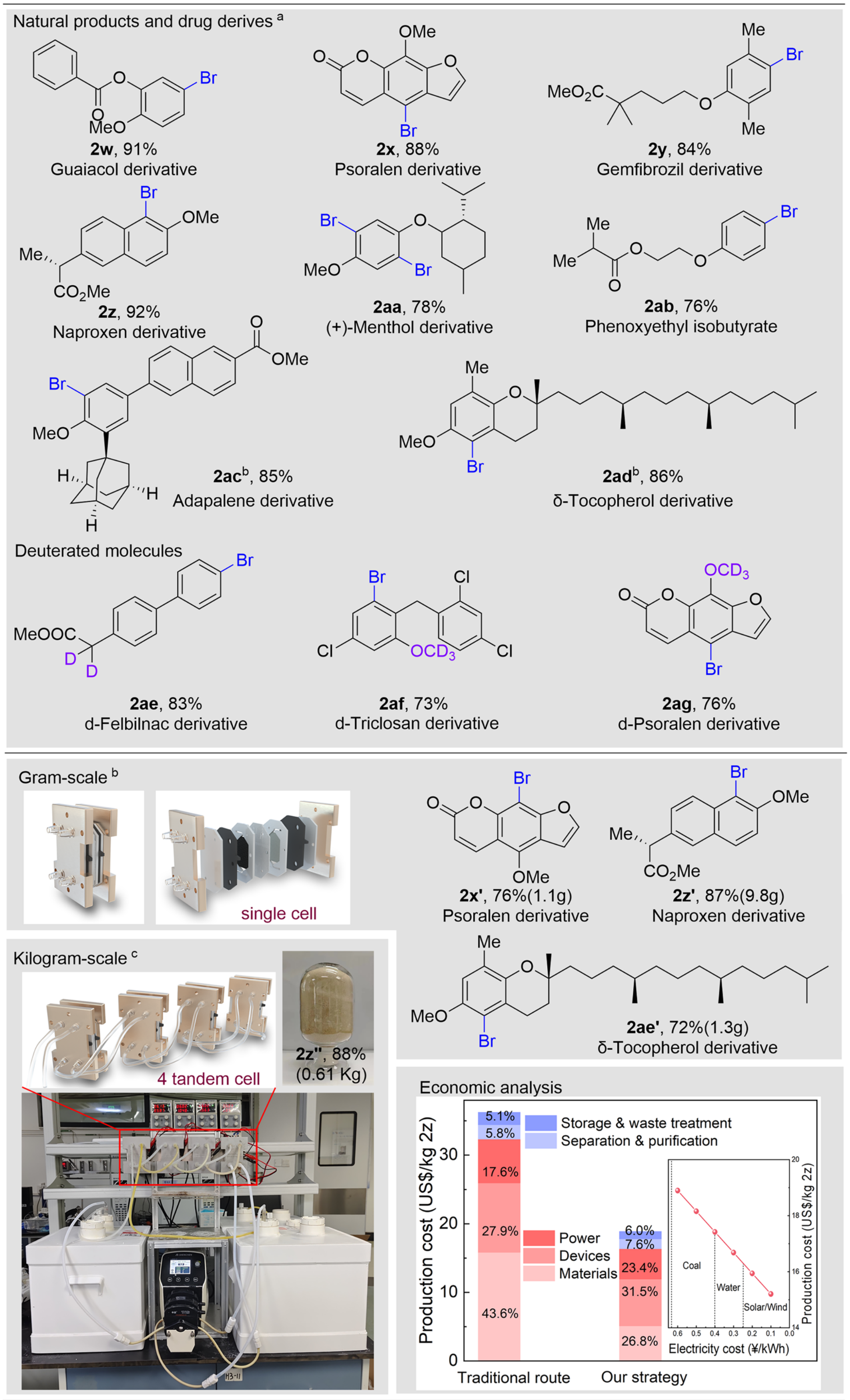

Fig. 5 | Direct bromination of natural products and drug derivatives. Reaction conditions: Co-O_V@CP (size: 10 mm × 10 mm × 0.3 mm) anode and carbon paper (size: 10 mm × 10 mm × 0.2 mm) cathode in an H-type cell divided by Nafion membrane, SCE as reference electrode; NaBr (0.5 M in deionized water, 12.5 mL), CH_3CN (12.5 mL) in each chamber, **1** (0.5 mmol), constant voltage (1.1-1.3 V vs. SCE) at room temperature for 4-8 h. Isolated yields are shown. [b]Reaction conditions: Co-O_V@ carbon felt (size: 35 mm × 30 mm × 5 mm) anode and carbon felt (size: 35 mm × 30 mm × 5 mm) cathode. Substrate (4 mmol), solvent (0.5 M NaBr in deionized water (10 mL): CH_3CN: CH_3OH: CH_2Cl_2 = 10:10:10:3), flow cell, two-electrode system and constant voltage (4-5 V), at room temperature, flow rate: 5 mL/min. Isolated yields are shown. [c]Reaction conditions: the same as condition *b* except for 4 tandem cells, constant voltage (6 V), 18 h, flow rate: 50 mL/min, 518 g substrate.

50% of the production cost, considering the compatibility of this method with solar power plant (Fig. 2i). In addition, we also conducted the experiments of in-situ electrochemical bromination of anisole using simulated brine (50 g L^{-1} Cl$^-$ + 3 g L^{-1} Br$^-$) as the electrolyte. LSV curves (Supplementary Fig. 24) show that the BER is more favorable than ClER on the Co_3O_4-O_V/CP catalyst with a ~ 0.2-V negatively shifted onset potential, even though the concentration of Cl$^-$ is remarkably higher than that of Br$^-$. This is a consequence of the lower theoretical potential of Br$^-$-to-Br_2 conversion (1.08 V vs. SHE) than that of Cl$^-$-to-Cl_2 conversion (1.35 V vs. SHE). Thus, a potentiostatic electrolysis can be conducted at around 1.1 V vs. SCE that only ignited BER but not ClER for in-situ electrochemical bromination reaction even in low-cost brine electrolytes.

With fast development of solar, wind or other green power technology, the further reduced electricity cost will enable a further 20% cost cut for the BER method in the near future (inset figure in Fig. 5 and Supplementary Fig. 23) and will achieve a sustainable and efficient bromine industry compared to traditional energy-intensive and environmentally unfriendly bromination method[10,11,46,47].

Discussion

In conclusion, we rationally designed and prepared oxygen-vacancy rich Co_3O_4 nanosheets on carbon paper to facilitate electrochemical BER in aqueous NaBr solution for on-site synthesis of value-added natural products and drug derivatives. The as-developed electrochemical synthesis process is efficient and sustainable with broad substrate scopes that is able to achieve kilogram-scale synthesis of drug derivatives. Our findings shall contribute to the design of thermodynamically favorable oxidation reactions coupled with hydrogen evolution to make value-added products in the carbon neutrality century.

Methods

Chemicals

Cobalt(II) nitrate hexahydrate (Adamas-beta Reagent Co., Ltd, RG, 99.9%), acetonitrile (Adamas-beta Reagent Co., Ltd, AR, 99%), sodium bromide (Aladdin, AR, 99%), anisole (Aladdin, GC, 99.9%), ultra-pure water (18.2 MΩ cm^{-1}, Millipore Corporation, Billerica), chloroform-D (Adamas, RG, 99.8 % D), and other chemicals were used as received without further purification.

Electrode preparation

Carbon paper (Shanghai Hesen Electric Co., Ltd., 0.2 mm thick) was cut into 10 × 20 mm^2 pieces and washed twice with deionized water and ethanol, respectively. After being dried in a vacuum oven, the tailored carbon paper was immersed in a 0.1 mol/L cobalt nitrate aqueous solution. Cyclic voltammetry (CV) from 0 V to -1.2 V vs. saturated calomel electrode (SCE) at a scan rate of 100 mV/s was then performed in a three-electrode configuration, in which carbon paper, platinum foil, SCE were used as the working electrode, counter electrode and reference electrode, respectively. After the reaction, the as-obtained carbon paper was rinsed with deionized water and calcined at 300 °C for 2 h in air (named as Co_3O_4@CP). To introduce oxygen vacancies onto Co_3O_4, the Co_3O_4@CP was calcined again at 300 °C for 15 min in 5% H_2/Ar atmosphere (named as Co-O_V@CP).

Characterization

The morphological information was obtained by scanning electron microscopy (SEM) (MIRA3, TESCAN). The TEM measurement was taken with a HITACH HT7700 microscope operated at an acceleration voltage of 80 kV. The crystal structure was characterized by X-ray diffraction (XRD) (Ultima IV, Rigaku) operated at 40 kV and 40 mA (Cu Kα X-ray radiation source) at a scanning speed and step interval of 6°/min and 0.01°, respectively. X-ray photoelectron spectroscopy (XPS) measurements were conducted on a Thermo Scientific K-Alpha XPS system using a monochromated Al Kα radiation. The inductively coupled plasma (ICP) emission experiments were conducted on an ICP-OES Optima 7000DV spectrometer (Perkin Elmer) or on an ICP-MS spectrometer (PerkinElmer NexION 300X). Electron Paramagnetic Resonance (EPR) tests were conducted on a BRUKER A300-10/12 instrument. Nuclear magnetic resonance (NMR) tests were performed on a Bruker AVANCE III NMR spectrometer (600 MHz). The organic products were analyzed by gas chromatography mass spectrometry (GC-MS, Agilent 7890 A) using 0.3 mmol toluene as the external standard. The high-resolution mass spectrometry (HRMS) was conducted by a Q Exactive GC Orbitrap GC-MS/MS (Thermo Scientific). In-situ surface-enhanced Raman spectra were recorded at the following applied potentials: 0.6 V, 0.8 V, 1.0 V, 1.2 V, and 1.4 V (vs. SCE) in 0.5 M NaBr aqueous solution at room temperature.

Electrochemical measurements

Linear sweep voltammetry (LSV) and cyclic voltammetry (CV) were carried out in an undivided cell filled with 0.5 mol/L NaBr aqueous solution mixed with an equal volume of acetonitrile. All electrochemical measurements were performed on a CHI 660E electrochemical workstation in a three-electrode configuration with glass carbon electrode, platinum foil, SCE as the working, counter, and reference electrode, respectively. The electrochemical synthesis of brominated chemicals was performed on Co-O_V@CP in a H-cell. Typical reaction conditions: each cell was filled with 7.5 mL acetonitrile and 7.5 mL 0.5 mol/L NaBr aqueous solution. 0.5 mmol substrate was dissolved in the anodic cel,l and constant voltage was applied. For large-scale production, DC power supply and carbon felt cathode was used.

DFT calculations

Spin-polarized density functional theory (DFT) calculations were performed using the Vienna ab initio Simulation Program (VASP)[48,49]. The electron exchange-correlation potential was treated by the Perdew-Burke-Ernzerhof (PBE) function[50] within the generalized gradient approximation. To simulate the adsorption of Br on Co_3O_4 surface, the preferred oriented crystallographic (110) plane of Co_3O_4 cubical phase as suggested from the TEM and XRD characterization, was constructed by a six-layer slab with a vacuum region of 20 Å along the *z*-axis to minimize the periodic image interactions. An energy cutoff was set to 520 eV to expand the wave functions. Brillouin zone integration was sampled with 2 × 3 × 1 Monkhorst-Pack[50] mesh *k*-points grids for geometry optimizations and 20 × 30 × 1 *k*-points grids for electronic property calculations of Co_3O_4 (110) slab, respectively. The outer valence electron arrangement of each element was set $2s^2 2p^4$ for O, $3d^7 4s^2$ for Co, $4s^2 4p^5$ for Br, respectively. DFT + U method was adopted with a typical U value of 3.4 eV for the consideration of the on-site Coulomb and exchange interactions of the strongly localized Co 3*d* electrons.

All geometries were fully optimized with the convergence tolerances set to be 0.015 eV/ Å for forces on all atoms. The energy corrections for the slab-to-slab dipole interaction along the surface perpendicular direction was employed[51,52]. The adsorption energy ($E_{*\mathrm{Br}}$) of Br on the Co_3O_4 surface was calculated as follows:

$$E_{*Br} = E_{Surf+Br} - E_{Surf} - 1/2E_{\mathrm{Br}_2}$$

where $E_{Surf+Br}$ is the total energy of Co_3O_4 (110) slab adsorbed with Br, E_{Surf} is the energy of the Co_3O_4 (110) surface and E_{Br_2} is the energy of the adsorbed bromine. Then, the free energy of the adsorbed state is calculated as:

$$\Delta G_{*Br} = \Delta E_{*Br} + \Delta E_{ZPE} - T\Delta S$$

where ΔE_{ZPE} is the difference corresponding to the zero point energy and ΔS is the entropy.

Data availability

The data that support the findings of this study are reported within the Article and its Supplementary Information and are available from the corresponding author upon request. Source data are provided with this paper.

References

1. Leow, W. R. et al. Chloride-mediated selective electrosynthesis of ethylene and propylene oxides at high current density. *Science* **368**, 1228–1233 (2020).
2. Saikia, I., Borah, A. J. & Phukan, P. Use of Bromine and Bromo-organic compounds in organic synthesis. *Chem. Rev.* **116**, 6837–7042 (2016).
3. Chai, S. et al. Comprehensive treatment technology of mother liquid from bromine extraction. *IOP Conf. Ser.: Earth Environ. Sci.* **859**, 012088 (2021).
4. Zhang, Y. et al. Development status and future development trend of bromine. *IOP Conf. Ser.: Earth Environ. Sci.* **300**, 032018 (2019).
5. Boldyryev, S. & Varbanov, P. S. Low potential heat utilization of bromine plant via integration on process and Total Site levels. *Energy* **90**, 47–55 (2015).
6. Dong, X., Roeckl, J. L., Waldvogel, S. R. & Morandi, B. Merging shuttle reactions and paired electrolysis for reversible vicinal dihalogenations. *Science* **371**, 507–514 (2021).
7. Song, S. et al. DMSO-catalysed late-stage chlorination of (hetero) arenes. *Nat. Catal.* **3**, 107–115 (2020).
8. Liang, Y., Lin, F., Adeli, Y., Jin, R. & Jiao, N. Efficient electrocatalysis for the preparation of (hetero)aryl chlorides and vinyl chloride with 1,2-Dichloroethane. *Angew. Chem. Int. Ed.* **58**, 4566–4570 (2019).
9. Yuan, Y. et al. Electrochemical oxidative clean halogenation using HX/NaX with hydrogen evolution. *iScience* **12**, 293–303 (2019).
10. Adimurthy, S. et al. Eco-friendly and versatile brominating reagent prepared from a liquid bromine precursor. *Green. Chem.* **8**, 916–922 (2006).
11. Adimurthy, S. et al. An alternative method for the regio- and stereoselective bromination of alkenes, alkynes, toluene derivatives and ketones using a bromide/bromate couple. *Green. Chem.* **10**, 232–237 (2008).
12. Huang, C., Huang, Y., Liu, C., Yu, Y. & Zhang, B. Integrating hydrogen production with aqueous selective semi-dehydrogenation of Tetrahydroisoquinolines over a Ni_2P bifunctional electrode. *Angew. Chem. Int. Ed.* **58**, 12014–12017 (2019).
13. Horn, E. J. et al. Scalable and sustainable electrochemical allylic C–H oxidation. *Nature* **533**, 77–81 (2016).
14. Kurimoto, A. et al. Bioelectrocatalysis with a palladium membrane reactor. *Nat. Commun.* **14**, 1814 (2023).
15. Zhang, B. et al. Electrocatalytic water-splitting for the controllable and sustainable synthesis of deuterated chemicals. *Sci. Bullet.* **66**, 562–569 (2021).
16. Taniguchi, I., Yano, M., Yamaguchi, H. & Yasukouchi, K. Anodic bromination of anisole in acetonitrile. *J. Electroanal. Chem. Inter. Electrochem.* **132**, 233–245 (1982).
17. Wu, Y. et al. Directing group enables electrochemical selectively meta-bromination of pyridines under mild conditions. *J. Org. Chem.* **86**, 16144–16150 (2021).
18. Xie, W. et al. Electrochemical regioselective bromination of electron-rich aromatic rings using nBu_4NBr. *Synlett* **30**, 1313–1316 (2019).
19. Raju, T. et al. Site directed nuclear bromination of aromatic compounds by an electrochemical method. *Tetrahedron Lett.* **47**, 4581–4584 (2006).
20. Jain, D. et al. Highly active nitrogen-doped carbon nanostructures as electrocatalysts for bromine evolution reaction: A combined experimental and DFT study. *J. Catal.* **413**, 1005–1016 (2022).
21. Cooper, W. D. & Parsons, R. Kinetics of the bromine/bromide electrode on platinum in aqueous sulphuric acid. *Trans. Faraday Soc.* **66**, 1698–1712 (1970).
22. Harrison, J. A. & Hermijanto, S. D. The oxidation of chloride ions and bromide ions on ruthenium dioxide electrodes. *J. Electroanal. Chem. Inter. Electrochem.* **225**, 159–175 (1987).
23. Wang, Y. et al. Distal Ruthenaelectro-catalyzed meta-C–H bromination with aqueous HBr. *Angew. Chem. Int. Ed.* **61**, e202201595 (2022).
24. Zhuang, Q. et al. Rich surface oxygen vacancies of MnO_2 for enhancing electrocatalytic oxygen reduction and oxygen evolution reactions. *Adv. Energy Sustain. Res.* **2**, 2100030 (2021).
25. Halder, S., Roy, S., Roy, S. & Chakraborty, C. Enriching oxygen vacancy in Co_3O_4 by solution combustion synthesis for enhanced supercapacitive property. *J. Phys. Chem. C* (2023).
26. Xu, L. et al. Plasma-engraved Co_3O_4 nanosheets with oxygen vacancies and high surface area for the oxygen evolution reaction. *Angew. Chem. Int. Ed.* **55**, 5277–5281 (2016).
27. Guan, S. et al. Oxygen vacancy excites Co_3O_4 nanocrystals embedded into carbon nitride for accelerated hydrogen generation. *Appl. Catal. B-Environ.* **269**, 118775 (2020).
28. Zeng, Y. et al. Co_3O_4 Nanocrystals with an oxygen vacancy-rich and highly reactive (222) facet on carbon nitride scaffolds for efficient photocatalytic oxygen evolution. *ACS Appl. Mater. Interfaces* **12**, 44608–44616 (2020).
29. Li, P. et al. Defect-engineered Co_3O_4 with porous multishelled hollow architecture enables boosted advanced oxidation processes. *Appl. Catal. B-Environ.* **298**, 120596 (2021).
30. Angelov, S., Zhecheva, E., Stoyanova, R. & Atanasov, M. Bulk defects in Co_3O_4, pure and slightly doped with lithium, revealed by EPR of the tetrahedral Co^{2+} ions. *J. Phys. Chem. Solids* **51**, 1157–1161 (1990).
31. He, Y. et al. Rare earth doping engineering tailoring advanced oxygen-vacancy Co_3O_4 with tunable structures for high-efficiency energy storage. *Small* **19**, 2206956 (2023).
32. Xiao, Z. et al. Operando identification of the dynamic behavior of oxygen vacancy-rich Co_3O_4 for oxygen evolution reaction. *J. Am. Chem. Soc.* **142**, 12087–12095 (2020).
33. Hu, W. et al. Electron-pinned defect-dipoles for high-performance colossal permittivity materials. *Nat. Mater.* **12**, 821–826 (2013).
34. Wang, Z., Wang, W., Zhang, L. & Jiang, D. Surface oxygen vacancies on Co_3O_4 mediated catalytic formaldehyde oxidation at room temperature. *Catal. Sci. Technol.* **6**, 3845–3853 (2016).
35. Cai, Z. et al. Single-crystalline ultrathin Co_3O_4 nanosheets with massive vacancy defects for enhanced electrocatalysis. *Adv. Energy Mater.* **8**, 1701694 (2018).
36. Wang, J. et al. Single-site Pt-doped RuO2 hollow nanospheres with interstitial C for high-performance acidic overall water splitting. *Sci. Adv.* **8**, eabl9271 (2022).
37. Wang, Y.-R. et al. Light, heat and electricity integrated energy conversion system: photothermal-assisted co-electrolysis of CO_2 and methanol. *Angew. Chem. Int. Ed.* **61**, e202212162 (2022).
38. Li, Y. et al. MoS_2 nanoparticles grown on graphene: an advanced catalyst for the hydrogen evolution reaction. *J. Am. Chem. Soc.* **133**, 7296–7299 (2011).
39. Li, T. et al. Ionic liquid in situ functionalized carbon nanotubes as metal-free catalyst for efficient electrocatalytic hydrogen evolution reaction. *Nanoscale* **13**, 4444–4450 (2021).
40. Wang, H.-Y. et al. In situ spectroscopic identification of μ-OO bridging on spinel Co_3O_4 water oxidation electrocatalyst. *J. Phys. Chem. Lett.* **7**, 4847–4853 (2016).
41. Wang, J. et al. Boosting the electrocatalytic activity of Co_3O_4 nanosheets for a Li-O_2 battery through modulating inner oxygen vacancy and exterior Co^{3+}/Co^{2+} ratio. *ACS Catal.* **7**, 6533–6541 (2017).
42. Lu, Y. et al. Engineering of cation and anion vacancies in Co_3O_4 thin nanosheets by laser irradiation for more advancement of oxygen evolution reaction. *Nano Energy* **83**, 105800 (2021).

43. Iliev, M. N. & Schmid, H. Raman spectroscopy of $M_3B_7O_{13}X$ boracites (M=Cr,Co,Ni,Cu,Zn,Cd; X=Cl,Br,I). *J. Raman. Spectrosc.* **45**, 267–273 (2014).
44. Agulló-Rueda, F., Calleja, J. M., Martini, M., Spinolo, G. & Cariati, F. Raman and infrared spectra of transition metal halide hexahydrates. *J. Raman. Spectrosc.* **18**, 485–491 (1987).
45. Bulusheva, L. G. et al. Effect of ultrasound pretreatment on bromination of double-walled carbon nanotubes. *Synth. Met.* **259**, 116233 (2020).
46. Na, J. et al. General technoeconomic analysis for electrochemical coproduction coupling carbon dioxide reduction with organic oxidation. *Nat. Commun.* **10**, 5193 (2019).
47. Zhao, B.-H. et al. Economically viable electrocatalytic ethylene production with high yield and selectivity. *Nat. Sustain.* **6**, 827–837 (2023).
48. Kresse, G. & Furthmüller, J. Efficiency of ab-initio total energy calculations for metals and semiconductors using a plane-wave basis set. *Comp. Mater. Sci.* **6**, 15–50 (1996).
49. Kresse, G. & Furthmüller, J. Efficient iterative schemes for ab initio total-energy calculations using a plane-wave basis set. *Phys. Rev. B* **54**, 11169–11186 (1996).
50. Perdew, J. P., Burke, K. & Ernzerhof, M. Generalized gradient approximation made simple. *Phys. Rev. Lett.* **77**, 3865–3868 (1996).
51. Makov, G. & Payne, M. C. Periodic boundary conditions in ab initio calculations. *Phys. Rev. B* **51**, 4014–4022 (1995).
52. Neugebauer, J. & Scheffler, M. Adsorbate-substrate and adsorbate-adsorbate interactions of Na and K adlayers on Al(111). *Phys. Rev. B* **46**, 16067–16080 (1992).

Acknowledgements

This work was financially supported by the National Key Research and Development Program of China (2021YFA1600800), National Natural Science Foundation of China (21972094, 22372102, 21902105, 22478348), Educational Commission of Guangdong Province (2021ZDZX2036), Shenzhen Science and Technology Program (RCJC20200714114434086), Research Team Cultivation Program of Shenzhen University (2023QNT013), National Postdoctoral Program for Innovative Talents (BX20180203), Shenzhen Science and Technology Program (20220811170440003), the City University of Hong Kong startup fund (9020003), ITF–RTH - Global STEM Professorship (9446006), and JC STEM lab of Advanced CO_2 Upcycling (9228005).

Author contributions

B.Z., B.L., and C.S. designed the idea. B.L. and C.S. supervised the project. B.Z., H.Y., Y. P., D.L. and C.Q. prepared and characterized the catalysts and electrodes. B.Z., W.L., and Y.F. conducted the electrochemical bromination reactions. B.Z., W.L., and Y.X. carried out the large-scale reactions. Z.L. conducted DFT calculations. B.Z., W.L., Y.P., D.L., J.D., and H.Y. finished the visualization work. B.Z., Y.P., L.Y., B.L., and C.S. conducted the economic analysis. B.Z., W.L., Z. L., B.L., and C.S. co-wrote the manuscript. All the authors discussed and commented on the manuscript.

Competing interests

The authors declare that they have no conflict of interest.

Additional information

Supplementary information The online version contains supplementary material available at https://doi.org/10.1038/s41467-025-57329-0.

Correspondence and requests for materials should be addressed to Bin Liu or Chenliang Su.

Peer review information *Nature Communications* thanks Nikolay Kornienko and the other anonymous reviewer for their contribution to the peer review of this work. A peer review file is available.

Reprints and permissions information is available at http://www.nature.com/reprints